Accepted for publication in the Astrophysical Journal
Preprint typeset using LaTeX style emulateapj v. 03/07/07

arXiv:0705.0003v2 [astro-ph] 12 Sep 2007

XO-2b: TRANSITING HOT JUPITER IN A METAL-RICH COMMON PROPER MOTION BINARY

Christopher J. Burke[1] P. R. McCullough[1], Jeff A. Valenti[1], Christopher M. Johns-Krull[2], Kenneth A. Janes[3], J. N. Heasley[4], F. J. Summers[1], J. E. Stys[1], R. Bissinger[5], Michael L. Fleenor[6], Cindy N. Foote[7], Enrique García-Melendo[8], Bruce L. Gary[9], P. J. Howell[3], F. Mallia[10], G. Masi[11], B. Taylor[3], T. Vanmunster[12]

(Received 2007 Sep 14)
Accepted for publication in the Astrophysical Journal

ABSTRACT

We report on a V=11.2 early K dwarf, XO-2 (GSC 03413-00005), that hosts a R_p=0.98$\pm^{0.03}_{0.01}$ R_J, M_p=0.57$\pm$ 0.06 M_J transiting extrasolar planet, XO-2b, with an orbital period of 2.615857$\pm$0.000005 days. XO-2 has high metallicity, [Fe/H]=0.45$\pm$0.02, high proper motion, μ_{tot} = 157 mas yr^{-1}, and has a common proper motion stellar companion with 31″ separation. The two stars are nearly identical twins, with very similar spectra and apparent magnitudes. Due to the high metallicity, these early K dwarf stars have a mass and radius close to solar, $M_\star = 0.98 \pm 0.02$ $M_\odot$ and $R_\star = 0.97\pm^{0.02}_{0.01}$ $R_\odot$. The high proper motion of XO-2 results from an eccentric orbit (Galactic pericenter, $R_{per} < 4$ kpc) well confined to the Galactic disk ($Z_{max} \sim 100$ pc). In addition, the phase space position of XO-2 is near the Hercules dynamical stream, which points to an origin of XO-2 in the metal-rich, inner Thin Disk and subsequent dynamical scattering into the solar neighborhood. We describe an efficient Markov Chain Monte Carlo algorithm for calculating the Bayesian posterior probability of the system parameters from a transit light curve.

Subject headings: binaries: eclipsing – planetary systems – stars: individual (GSC 34130-0005) – techniques: photometric – techniques: radial velocities

1. INTRODUCTION

We announce the discovery of an extrasolar planet, XO-2b, that transits a bright, V=11.2, star. With an orbital period, $P \sim 2.6$ days, planetary radius, R_p =0.98 R_J, and planetary mass, M_p =0.57 M_J, XO-2b belongs to the growing class of transiting Hot Jupiter (HJ) planets (Charbonneau et al. 2007). Despite the increasing number of transiting planets known, much work still remains to understand the observed properties of planets. The transiting planets HD209458b (Charbonneau et al. 2000; Henry et al. 2000), HAT-P-1b (Bakos et al. 2007), and WASP-1b (Cameron et al. 2007; Charbonneau et al. 2007b) have anomalously large radii compared to theoretical models and are thought to require an external source of energy to remain inflated (Bodenheimer et al. 2003; Guillot & Showman 2002; Winn & Holman 2005). However, recently Burrows et al. (2006) explain the radii of transiting planets without the need for an extra source of energy by accounting for enhanced metallicity opacities and properly comparing observed radii to theoretical radii. In contrast, HD149026b has an extremely high density and small radius (Sato et al. 2005). There is general agreement that a pure H/He mixture cannot explain the small radius of HD149026b, but a planet model with a massive central core, $M_c \sim 70$ $M_\oplus$, of heavy elements along with a small H/He envelope can explain the radius of HD149026b (Sato et al. 2005; Fortney et al. 2006).

Disentangling the effects of stellar irradiation, migration, central core mass, and composition on the observed properties of planets requires discovering more bright transiting planets (Charbonneau et al. 2007; Fortney et al. 2006). XO-2b is the second contribution to the bright transiting planet sample provided by the XO Project (McCullough et al. 2005); XO-1b being the first (McCullough et al. 2006). Of the bright transiting planet hosts ($V < 12$), XO-2 has the highest metallicity ([Fe/H]=0.45 see § 3.1). In addition, from a recent catalog of extrasolar planets (Butler et al. 2006), XO-2 has a higher metallicity than 96% of all known extrasolar planet hosts.

Metallicity plays a crucial role in the formation of planets and the resulting HJ atmospheres. The frequency of radial velocity detected planets is known to increase with metallicity (Fischer & Valenti 2005). In the core accretion planet formation model, a high metallicity environment grows larger cores and enables more objects to reach the critical mass necessary for runaway gas accretion and transformation into a detectable gas giant planet (Ida & Lin 2004; Benz et al. 2006). Detailed fits to the mass and radius of the known transiting planets yields a mass estimate for the central refractory element core (Guillot et al. 2006; Burrows et al. 2006). These investigations derive a larger core mass for planets that transit higher metallicity stars. In addition to the bulk properties of extrasolar planets, metallicity plays an important role in the planet's atmosphere, especially for a

Electronic address: cjburke@stsci.edu
[1] Space Telescope Science Institute, 3700 San Martin Dr., Baltimore MD 21218
[2] Dept. of Physics and Astronomy, Rice University, 6100 Main Street, MS-108, Houston, TX 77005
[3] Boston University, Astronomy Dept., 725 Commonwealth Ave.,Boston, MA 02215
[4] Inst. for Astronomy, University of Hawaii, 2680 Woodlawn Dr., Honolulu, HI 96822-1839
[5] Racoon Run Observatory, Pleasanton, CA
[6] Volunteer Observatory, Knoxville, TN
[7] Vermillion Cliffs Observatory, Kanab, UT
[8] Esteve Duran Observatory Foundation, Montseny 46, 08553 Seva, Spain
[9] Hereford Arizona Observatory, Hereford, AZ
[10] Campo Catino Astronomical Observatory, Guarcino, Italy
[11] Virtual Telescope Project, Bellatrix Astronomical Observatory, Ceccano, Italy
[12] CBA Belgium Observatory, Landen, Belgium

HJ experiencing large stellar irradiation. An increased metallicity results in a greater absorption of the stellar irradiation and larger equilibrium temperatures than a comparable planet of lower metallicity (Fortney et al. 2006). The variations in equilibrium temperature can lead to variations in the dominant observable features in the planet's atmosphere.

Amongst the other transiting HJ planets, XO-2b shares a common characteristic with another transiting HJ, HAT-P-1b (Bakos et al. 2007). Both planets orbit one member of a nearly-equal-mass, wide separation stellar binary. The XO-2 stellar binary system has a separation of 31″ ($\sim$ 4600 AU separation with a distance of $\sim$ 150 pc) and both components have an identical within the uncertainties 157 mas yr^{-1} proper motion vector as measured with Tycho-2 (Høg et al. 2000) and the high proper motion catalog of (Lépine & Shara 2005). It is not unusual for planets to exist in binary systems. Raghavan et al. (2006) find >23% of stars with planets have a stellar companion, however, they find evidence that the extrasolar planet sample is deficient in stellar binaries when compared to the field. A stellar companion with a 4600 AU separation is not expected to influence the planet formation process. Even assuming an orbital eccentricity, e=0.8, for the unknown eccentricity of the XO-2 stellar binary, planets within $a_c \sim 170$ AU of XO-2 are dynamically stable (Holman & Wiegert 1999) (we assume the current measured projected binary separation is close to the actual semi-major axis of the orbit when calculating a_c). Empirically, Desidera & Barbieri (2007) do not find any statistically significant difference between planets around single stars and planets in wide ($a > 100$ AU) separation binaries. However, understanding the influence of a stellar companion on the planet formation process is complicated by the fact that the binary configuration during planet formation may be vastly different than what is currently observed (Marzari & Barbieri 2007; Malmberg et al. 2007).

The similar brightness of the XO-2 stellar binary components and their angular separation provides an excellent opportunity for detailed line abundance studies. The higher metallicity of the known planet host stars is thought to be of primordial origin rather than heavy element pollution due to infalling planets (Fischer & Valenti 2005; Gonzalez 2006). The infalling planet model for explaining the higher metallicity of the known planet host stars has predominately come from observations showing differing element abundances between common proper motion binary components. These element abundance differences have typically been overturned by further independent analyses (Gonzalez 2006). The difficulty in reliable abundance differences results from systematic effects in analyzing stars of different T_{eff} and evolutionary state (Schuler et al. 2006). Such effects are reduced for the XO-2 stellar binary.

On the sky, XO-2 and a line joining its stellar companion has a position angle of 162°, nearly along the North-South direction (see the finder chart in Figure 1). XO-2 is the Northern component of the binary (indicated by the arrow in Figure 1). The magnitude difference between the components is $\Delta V = 0.05$ mag. Thus, in the optical, XO-2 is fainter than its Southern companion. The traditional nomenclature for binary stars designates XO-2 as XO-2B and the planet XO-2Bb. However, throughout

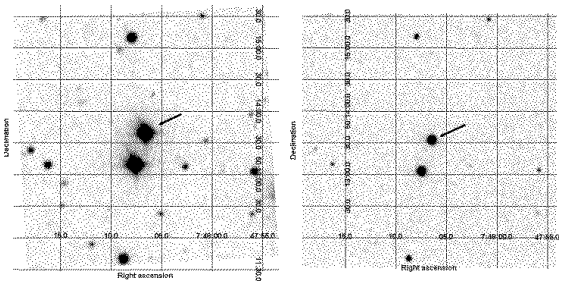

FIG. 1.— Finder chart for XO-2 and its stellar companion at two epochs. The arrow indicates XO-2. North is toward the top of the figure and East is toward the left of the figure. (*Left*) Digital Sky Survey POSS I Red image from 1953. (*Right*) 2MASS H-band image from 2000. The common proper motion is predominately directed South.

this article we simply designate the transiting HJ stellar host XO-2 and the planet around it XO-2b. When it is unclear from the context we alternatively designate XO-2 as XO-2N and the Southern stellar companion as XO-2S. We adopt this naming convention because the magnitude difference between the stellar components is small and the spectra are nearly identical, both of which make it difficult to distinguish the objects, whereas the 31″ separation readily distinguishes the stellar components based on declination. We refer to both stellar components as a unit as the XO-2 stellar binary.

In § 2, we provide details of the discovery and follow up photometry and spectroscopy. The high resolution spectroscopy is analyzed in § 3.1 to determine the stellar properties of XO-2N and XO-2S. The high precision photometry is analyzed in § 3.2 employing an efficient Markov Chain Monte Carlo (MCMC) algorithm to determine the properties of XO-2b. We confirm the planetary mass of XO-2b with radial velocity measurements in § 3.3. The ephemeris for XO-2b is refined and the transit observations are investigated for transit timing variations in § 3.4. There is a brief discussion regarding the XO-2 stellar binary and its Galactic orbit in § 4, and we summarize the article in § 5.

2. OBSERVATIONS

2.1. *XO Project Photometry*

XO-2b is the second transiting planet discovered by the XO survey after XO-1b (McCullough et al. 2006). McCullough et al. (2005) and McCullough & Burke (2007) describe the instrumentation, operation, and analysis in more detail than the summary provided here. The twin, 200mm XO cameras power drift scan in declination over a 7 deg $\times$62 deg strip every ten minutes on clear nights for more than 2 months per season of visibility. The XO observations employ a broad (0.4μm to 0.7μm) passband. The star XO-2 comes from the XO strip centered on RA 8.0 hr and is one of several thousands of bright (V< 12) stars monitored in this strip over the period September 2003 to September 2005. The Box-fitting Least Squares algorithm, BLS, (Kovács et al. 2002) was employed to search the nearly 3000 observations per star for repetitive transit events with periods ranging from $P = 0.5 - 10$ day. We perform the transit search on two realizations of the light curve. One realization is the calibrated light curves as described in McCullough et al. (2005) and the other realization of the light curve has the SysRem algorithm (Tamuz et al. 2005) applied to the calibrated light curve in order to fur-

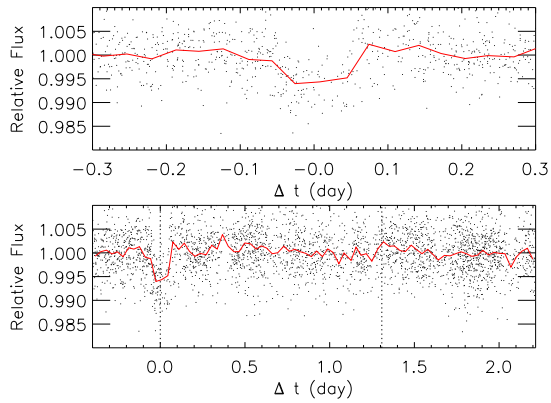

FIG. 2.— Discovery phased light curve from the XO Project data. (*Top*) The phased light curve around the transit event. (*Bottom*) The phased light curve over the full orbital period. The individual measurements (*points*) are shown binned (*solid line*) to reduce noise. The transit occurs at $\Delta t = 0.0$ day and any secondary eclipse for a circular orbit would occur at $\Delta t = 1.3$ day (*dotted line*). No secondary eclipse is evident above the noise. At the resolution of the XO cameras, both components of the XO-2 stellar binary are within the photometry aperture causing dilution of the transit depth.

ther remove systematics. In the case of XO-2, there were no substantive improvements in the light curve quality after implementing SysRem and both analyses identified the same transit period and phase.

McCullough & Burke (2007) describe the selection of transit candidates for followup. In addition, for consideration the candidates must pass selection criteria as described in Burke et al. (2006). In brief, we require observations covering more than 1.5 transit events, avoid 0.5 and 1.0 day periods where systematic aliases result in false-positive detections, require the transit depth, $\delta m < 0.1$ mag, and require the transit to have higher significance than systematic errors (as measured by the transit to anti-transit Ratio Statistic, RS, of Burke et al. (2006)).

Figure 2 shows the XO light curve phased on the detected period as returned from BLS. We achieved 0.7% or 0.007 mag per observation precision on this V=11.2 object. The transit occurs at $\Delta t = 0.0$ day and any signature of a secondary eclipse would occur at $\Delta t = 1.3$ day for a circular orbit. At the angular resolution of the XO survey, both components of the XO-2 stellar binary are within the photometry aperture leading to transit depth dilution. Light curves resolving the components of the XO-2 stellar binary result in twice the transit depth (see Figure 3), but in the discovery light curve the transit depth is 0.007 mag. With the XO cameras, we observed two nearly complete transits of XO-2b at the end of 2004, and beginning of 2005 (Julian dates 2453355 and 2453376). In addition, on seven other nights, XO cameras captured partial ingress and egress events. First occurrence of a partial transit was at the end of 2003 on Julian date 24552994. Table 1 provides a sample of the photometry for XO-2 from the XO cameras. The full table is available in the online edition.

2.2. *Extended Team and Follow Up Photometry*

The Extended Team (E.T.) provides photometric follow up for XO candidates. The E.T. (R. B., M. F., C. F., E. G-M.,B. G., P. H., F. M., G. M., and T. V.) is a collaboration of professional and amateur astronomers (McCullough et al. 2005, 2006). We sent the candidate list containing XO-2 to the E.T. on January 16, 2007. On, January 18, 2007, E.T. observations confirmed the transit events for XO-2b in the R-band using a 0.6-m telescope (solid green line in Figure 3). The initial observations were truncated due to high air mass, but the observations confirmed the XO ephemeris, the transit occurs in the Northern star of the XO-2 stellar binary, and the undiluted transit depth is consistent with a planetary radius and the XO photometry. A complete transit was observed by the E.T. on January 26, 2007 and the binned R-band light curve obtained with a 0.35-m telescope is shown as the solid red line in Figure 3. The light curves shown in Figure 3 are used for refining the ephemeris and looking for evidence of transit timing variations in § 3.4. Based on observations of other transit candidates by the E.T., repeat transit events in the same passband have a 0.2% or 0.002 mag standard deviation in deriving the transit depth. At this level of precision, the E.T. observations of XO-2b are consistent with a gray transit. Table 1 provides E.T. photometry for XO-2. For the E.T. light curves, the median differential magnitude out of transit provides the flux normalization and the standard deviation out of transit provides the uncertainty in the measurements.

On February 16, 2007 we observed a transit event of XO-2b with the 1.83-m Perkins Telescope at Lowell Observatory using the PRISM instrument in imaging mode (Janes et al. 2004). The PRISM camera is a 2048x2048 Fairchild CCD with 0.39″/pix resolution. The transit event was well positioned in the evening, occurring over the airmass range $1.05 \lesssim X \lesssim 1.16$. To improve efficiency a subframe containing XO-2N and XO-2S was read out with a 8-10 s cadence. The average seeing during the course of observations, 3″, was poor for the site. The final light curve is a differential light curve for XO-2N using XO-2S as the comparison shown in Figure 4 employing aperture photometry and an R-band filter. The selected aperture size for photometry minimizes the resulting rms scatter in the differential light curve. In addition to the R-band photometry, photometry in the BVI passbands was obtained before the transit, at mid-transit, and after the transit. The gap in the R-band data at mid-transit accommodates the multiple filter data. A computer failure resulted in the gap of R-band data at the start of ingress.

To normalize the differential light curve, the average magnitude from out of transit data was subtracted from the light curve. This was done independently for each half of the light curve separated by the mid-transit gap. There is a $\Delta m = 0.001$ magnitude difference in the normalization zeropoints between the data before and after the transit. This offset results from repositioning the telescope and refocusing for the BVI data acquisition at mid-transit. During an uninterrupted R-band data series, a 0.3 pix rms positional accuracy was maintained resulting in ∼0.0014 mag rms over 1 minute intervals. Accurate positioning was not maintained for the BVI data resulting in $\sim \Delta 0.005$ mag offsets between the data obtained before and after the transit. The average BVI passband data before transit was subtracted from the BVI data obtained at mid-transit and after transit to yield the differential light curve in these passbands as shown in Figure 4. Within the systematics resulting from

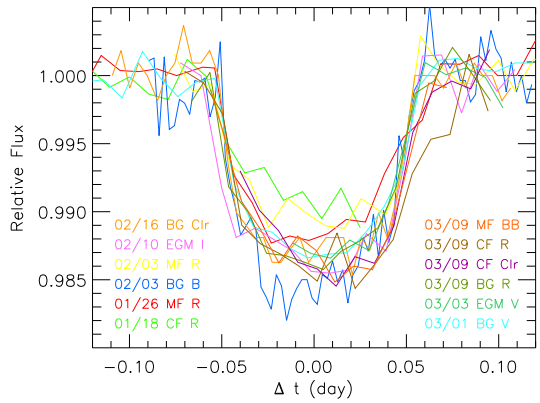

FIG. 3.— Binned light curves from the Extended Team for XO-2. The color of the text in the lower left corner indicates the date (2007), observer, and passband of the observations. The passband labels are Johnson for the system except *Clr* indicates unfiltered observations and *BB* indicates a blue blocking (> 0.5 μm) filter.

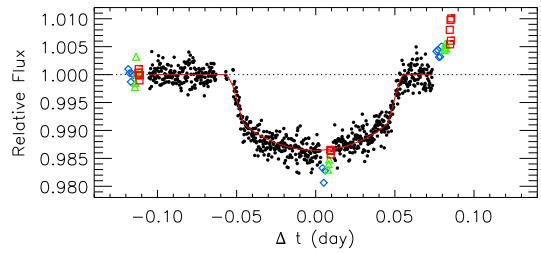

FIG. 4.— Light curve from the 1.8m Perkins Telescope at Lowell Observatory in the R-band (*points*) for XO-2N using XO-2S as the comparison star. The open symbols show the differential photometry in the B (*diamond*), V (*triangle*), and I (*square*) passbands using the average of the BVI observations obtained before the transit for the flux normalization level (*dotted line*). Accurate positioning of the stellar image on the detector was not maintained during the BVI observations resulting in 0.5% or 0.005 mag systematic offsets. However, accurate positioning of the stellar image on the detector was maintained during the R-band light curve resulting in ∼0.0014 mag rms over 1 minute intervals. Also shown is the best-fit transit model in a χ^2 sense during the MCMC analysis. (*solid line*).

repositioning of the stars on the detector, the transit is gray.

We obtained photometric B, V, R_C, and I_C magnitudes for XO-2N and XO-2S using a 0.35-m telescope on the photometric night of January 24, 2007 (Table 2). A single Landolt area (Landolt 1992) was observed at the same airmass as XO-2 to derive the zero point and color transformation coefficients. The color transformation coefficients were consistent with comprehensive standard star measurements from four Landolt fields obtained two weeks previous using the identical instrumental setup. The color range of Landolt standards was $-0.14 \leq (B - V) \leq 1.4$. The B, V, R_C, and I_C absolute photometric accuracies are 0.04, 0.04, 0.04, and 0.05 mag r.m.s., including both the rms scatter around the photometric transformation model and an estimated systematic error. The Tycho-2 magnitudes for XO-2 listed in Table 2 transform (via Table 2 of Bessell (2000)) to Johnson $V = 11.25$, i.e. 0.07 mag (2-σ) fainter than our estimate. In addition, we accurately measured the instrumental magnitude difference between XO-2N and XO-2S. We find XO-2N is fainter than XO-2S by 0.07±0.008 mag in the B-band, 0.055±0.004 mag in the V-band, 0.040±0.004 mag in the R-band, and 0.030±0.003 mag in the I-band.

2.3. *Spectroscopy*

After confirmation of the XO transit light curve from E.T. observations (see §2.2), we initiated queue schedule observations of XO-2N and XO-2S with the High-Resolution Spectrograph (HRS), a fiber fed cross-dispersed echelle spectrograph (Tull 1998), on the McDonald Observatory 11-m Hobby-Eberly Telescope (HET) in order to measure the mass of the planet. The first HRS observations using an iodine gas cell for precision radial velocities commenced on January 26, 2007. Table 3 provides dates of the HRS observations along with the resulting radial velocities. The instrument setup provides R=60,000 resolution and wavelength coverage over the range $4000 < \lambda < 7800$ Å with center at $\lambda = 5900$ Å. We extracted the two-dimensional echelle spectra using procedures described in Hinkle et al. (2000). The resulting Signal-to-Noise ratio (SNR) varied from 20-50 per extracted pixel at the blaze peak. We calculate radial velocities for XO-2N and XO-2S in § 3.3.

To measure the stellar parameters of XO-2N and XO-2S, we also obtained spectra with the 2dCoudé echelle spectrometer (Tull et al. 1995) on the McDonald Observatory 2.7-m Harlan J. Smith Telescope (HJS). We obtained two spectra of XO-2N and a single spectrum of XO-2S with R=60,000 and wavelength coverage of 3900-9600 Å. We determine the stellar parameters in § 3.1.

3. ANALYSIS

3.1. *Stellar Properties*

We use the Spectroscopy Made Easy (SME) analysis package of Valenti & Piskunov (1996) with refinements from Valenti & Fischer (2005) on the HJS spectra to measure the stellar properties of XO-2N and XO-2S. We briefly describe the process here. The free parameters, T_{eff}, log$g$, [M/H], $v \sin i$, [Na/H], [Si/H], [Ti/H], [Fe/H], and [Ni/H], are varied in order to minimize the difference of the resulting synthetic spectrum to the observed spectrum. A quadratic continuum is fit over 8 wavelength intervals for each unique set of the above free parameters. When generating the synthetic spectrum, the pressure-temperature profile of the atmosphere comes from interpolating the atmosphere grid of Kurucz (1992). The atomic line list comes from the Vienna Atomic Line Database (VALD) (Piskunov et al. 1995) and the molecular line list comes from Kurucz (1993). The line strengths and van der Waals damping parameter of the line list database were adjusted to improve agreement with the observed solar spectrum, as described in Valenti & Fischer (2005).

Table 4 lists the stellar parameters for XO-2N and XO-2S based on the SME analysis. The results for XO-2N are based on the average from two spectra and the results for XO-2S are based on a single spectrum. Both XO-2N and XO-2S independently result in a metal enhanced abundance, [Fe/H]=0.45±0.02. Using the primary observables from the SME analysis (T_{eff}, abundances, and log$g$) and the apparent magnitude in the V-band (§ 2.2), we determine secondary stellar properties, $M_\star$, $R_\star$, dis-

tance, and age using the Y^2 isochrones (Yi et al. 2001) following the procedure of Valenti & Fischer (2005). The distance to XO-2 is unknown, thus the probability density function for $M_\star$, $R_\star$, and age are calculated for a sequence of trial distances in steps of 10 pc. The SME isochrone analysis for select distances to XO-2 are listed in Table 5. We determine a distance, d=150 pc, to XO-2 in § 3.2 from a joint analysis of the SME analysis and transit light curve. We show the probability density for the XO-2N parameters in Figure 5 for the preferred distance to XO-2 of 150 pc.

The spectrum alone yields an estimate of the stellar gravity, $\log g_{sme}$. Estimates of $M_\star$ and $R_\star$ from the isochrone analysis provide an additional estimate of $\log g_{iso}$ as a function of distance to XO-2. The condition $\log g_{sme}$=$\log g_{iso}$ yields an approximate distance to XO-2. The data for XO-2S provides a consistency check, and ideally the condition $\log g_{sme}$=$\log g_{iso}$ for XO-2S is met for the same distance as XO-2N. In practice, we find XO-2S has $\log g_{sme} = 4.6$; too large a value for $\log g_{iso}$ to accommodate at any distance. Also, XO-2S being brighter and thus more massive than XO-2N implies $\log g_{sme}$ for XO-2S should be lower than $\log g_{sme} = 4.5$ of XO-2N, opposite of what is measured. Analysis of the transit light curve along with the physical parameters for XO-2N from the isochrone analysis in § 3.2, yields $\log g_{lc,iso} \sim 4.5$, confirming the spectroscopic $\log g_{sme}$ for XO-2N is correct and the $\log g_{sme}$ for XO-2S is an overestimate.

The overestimate in $\log g_{sme}$ for XO-2S is not without precedent. The SME based $\log g$ can result in higher values than the Y^2 isochrones allow for some objects in the Spectroscopic Properties of Cool Stars (SPOCS) catalog as a result of the numerous degeneracies that exist between the spectral parameters (see Figure 16 of Valenti & Fischer (2005)). Despite individual cases of an overestimated $\log g$, comparing stars analyzed with SME in common with other independent spectral analyses does not reveal a systematic offset in $\log g$ (see Figure 20 of Valenti & Fischer (2005)). The 1-σ uncertainties in the stellar parameters given in Table 4 are based on the typical rms scatter in parameters measured in independent, multiple spectra for stars in the SPOCS catalog. Based on the 1-σ uncertainties in Table 4, the difference in $\log g$ between XO-2N and XO-2S is significant. However, the distribution of repeat measurements for parameters in the SPOCS catalog (see Table 5 of Valenti & Fischer (2005)) display extended wings and the Gaussian-based uncertainties underestimate the possibility of outlying measurements. Thus, we also provide the 99.7% confidence intervals for the parameters based on Table 5 of Valenti & Fischer (2005). Since, the XO-2S parameters are based on a single spectrum, the 99.7% confidence interval is more appropriate than relying solely on the 1-σ error when deciding on the significance of any differences between the properties of XO-2N and XO-2S.

3.2. *Markov Chain Monte Carlo Light Curve Analysis*

Ford (2005), Gregory (2005), and references therein provide a thorough discussion of the theory behind Markov Chain Monte Carlo (MCMC) Bayesian analysis along with a practical MCMC implementation for radial velocity planet detection. In a multidimensional problem, the MCMC algorithm is an efficient means of calculating the Bayesian posterior probability for parameters. Holman et al. (2006) describe MCMC analysis applied to determining the system properties for transiting extrasolar planets. In their analysis of the transit light curve for XO-1b, Holman et al. (2006) calculate the posterior probability using the stellar radius, $R_\star$, planet radius, R_p, orbital inclination, i, and the two coefficients of the quadratic limb darkening law as free parameters. In the transit fitting problem, the relationship between $R_\star$, R_p, and i has a high degree of degeneracy and nonlinearity. We illustrate the degeneracy and nonlinearity between parameters in the top panels of Figure 6 for a MCMC calculation of the XO-2b system properties. The nonlinear, "banana-shaped" degeneracy between R_p and i slows the rate of convergence for MCMC algorithms. MCMC algorithms work more efficiently when the relationship between parameters is multi-normal without covariance (Kosowsky et al. 2002).

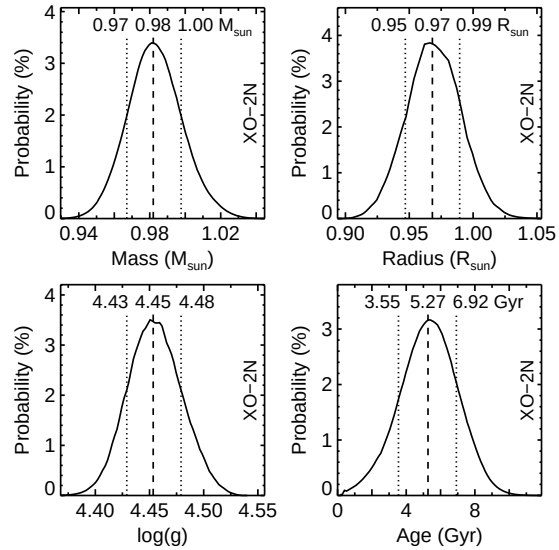

FIG. 5.— Distributions for four stellar parameters derived from the SME analysis (see text) for a distance of 150 pc. The values of the mean and limits containing ±34% of the distribution from the mean are annotated on the figures and listed in Table 4 along with corresponding values for distances of 140 pc and 170 pc.

To remove the nonlinearity between parameters, we choose the following set of free parameters: $R_\star$, $\rho = R_p/R_\star$, and the total transit duration from $1^{\rm st}$ to $4^{\rm th}$ contact, τ. With this nonlinear transformation, the degeneracy between the new set of parameters is along a straight line as shown in the middle panels of Figure 6. A further linear transformation between parameters yields an eigenbasis set of parameters with a multi-normal non-covariant relationship that results in an efficient MCMC calculation. These transformations improve the rate of convergence for the MCMC analysis by more than a factor of 100 when measured by the autocorrelation length of the samples in the MCMC sequence. Appendix A provides further details of the MCMC implementation developed for this study.

We employ the Metropolis-Hastings algorithm with a normal proposal distribution for calculating the Markov Chain. We follow a Gibbs-like sampling technique where each step in the chain consists of a number of intra steps updating each individual parameter in turn. Several short, trial chains iteratively yield scale factors of the

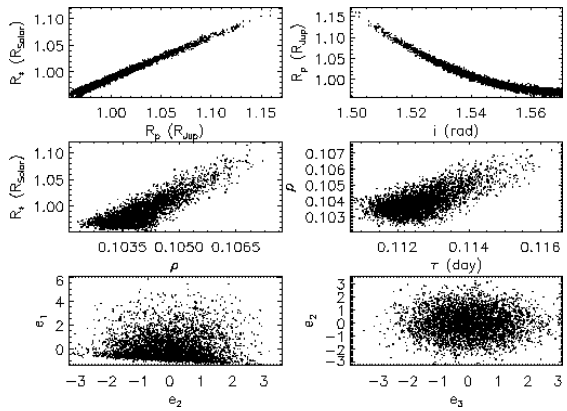

FIG. 6.— Correlation between parameters for samples in a MCMC calculation of the XO-2b posterior distribution. The parameters $R_\star$, R_p, and i are tightly correlated and the R_p versus i correlation is nonlinear (*Top*). With the choice of parameters, $R_\star$, ρ, and τ, the correlations between parameters are linear (*Middle*). Solving for the eigenvectors of the covariance matrix from samples shown in the Middle Panel yields an eigenbasis set of parameters (*Lower*). The eigenvector along the direction of largest variance, e_1 is predominately along $R_\star$. Eigenvectors e_2 and e_3 are a mixture of ρ and τ. The multi-normal without covariance properties of the eigenbasis set of parameters provides a more efficient MCMC calculation.

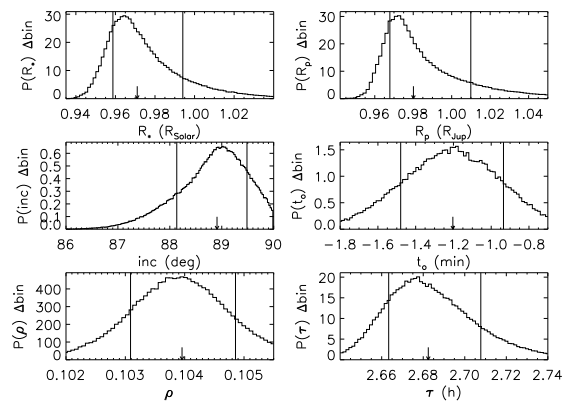

FIG. 7.— Marginalized posterior probability for the XO-2 and XO-2b parameters from MCMC samples. We adopt the median of the posterior probability (*arrow*) as the point estimate of the parameter. The *solid* lines indicate the 68.3% credible interval.

normal proposal distribution for each parameter with a 25% to 40% acceptance rate for the trial samples. The likelihood function is given by $e^{-0.5\chi^2}$, were we have assumed the errors are normally distributed, and the data have uniform weights. χ^2 is the squared difference between observations and the analytic transit model of Mandel & Agol (2002). The model assumes negligible eccentricity. The observations are the R-band data from the 1.8m Perkins Telescope shown in Figure 4.

The calculation has seven free parameters: $M_\star$, $R_\star$, ρ, τ, t_o, u_1, and u_2. t_o is the mid-transit time offset from the ephemeris with a period given by the XO observations and a mid-transit zeropoint near the mid-transit gap of the light curve, HJD 2454147.75. The limb darkening coefficients, u_1 and u_2, model the limb darkening with the quadratic law, $I = 1-u_1(1-\mu)-u_2(1-\mu)^2$, where I is the specific intensity normalized to unity at the center of the stellar disk and μ is the cosine of the angle between the line of sight and the surface normal. In practice, we follow Holman et al. (2006) by adopting $a_1 = u_1 + 2u_2$ and $a_2 = 2u_1 - u_2$ as the parameters used in the calculation. This linear combination of limb darkening coefficients reduces their mutual degeneracy.

The prior for $R_\star$, ρ, and τ is given by Equation A5, which is equivalent to a prior uniform in $R_\star$, R_p, i. The priors for $R_\star$, ρ, and t_o have cutoff values well beyond values allowed by the data. The prior on τ has an upper limit cutoff, $\tau < \tau_{max}$, where τ_{max} is the longest transit duration possible for a given $R_\star$, $M_\star$, and ρ. We assume uniform priors for the limb darkening coefficients with the following physically motivated limits on the parameters. We require the highest surface brightness to be located at the disk center ($u_1 \geq 0.0$), require the specific intensity to remain above zero ($u_1 + u_2 \leq 1.0$), and do not allow limb-brightened profiles ($u_1 + 2u_2 \geq 0.0$). The form of the prior for $M_\star$ is a Gaussian where the central value and standard deviation of the Gaussian are a function of $R_\star$ as given by the SME isochrone analysis data given in Table 5 and described in § 3.1. We employ a spline interpolation over the grid of $M_\star$ and σ_M as a function of $R_\star$.

The estimate of the posterior probability comes from 7 independent chains of length $N_{chn} = 60000$ with varying initial conditions. This results in an effective length $N_{eff} = N_{chn}/N_{cor} = 12000$ after taking into account the autocorrelation length $N_{cor} = 5$. Using these 7 chains, the largest Gelman-Rubin statistic amongst the parameters, R=1.0002, where R<1.02 indicates convergence of the chain (Gelman & Rubin 1992). Figure 7 shows the resulting posterior probability distribution for each parameter after marginalization over the other parameters. The posterior probability is simply a normalized histogram of the MCMC sample values. We adopt the median as the best single point estimate of the posterior probability. To derive an α% credible interval for a parameter, the N MCMC samples are sorted by the parameter of interest. The lower limit of the credible interval is taken as the $((1-\alpha)/2)N^{\rm th}$ sorted sample, and the upper limit of the credible interval is taken as the $(1-(1-\alpha)/2)N^{\rm th}$ sorted sample. The arrow point along the abscissa in Figure 7 indicates the median of the posterior probability, and the the vertical solid lines in Figure 7 show the 68.3% credible interval.

Figure 8 shows the joint posterior probability for the stellar limb darkening coefficients, u_1 and u_2. The solid contours are isoprobability contours containing 68% and 90% of the MCMC samples. The small points illustrate the remaining 10% of the samples lying outside the region of highest probability. The region of highest probability for the limb darkening coefficients differs from the theoretically calculated limb darkening coefficients (open triangle symbol) obtained from Claret (2000). The dash lines illustrate the prior limits for the limb darkening coefficients. The lower dash line in Figure 8 corresponds to not allowing limb brightened specific intensity profiles.

Using the SME isochrone analysis, we translate the MCMC samples for $R_\star$ into distance to XO-2 and age estimates. Similar to the procedure that defines the prior on $M_\star$, we interpolate the $R_\star$ versus trial distance and age relationships given by the SME isochrone analysis (i.e., for a given stellar radius estimate, the SME isochrone analysis has a best distance and age estimate for the system). The posterior probability for these two parameters is shown in Figure 9. We repeated the calculation assuming a prior uniform in $\cos i$, and this did

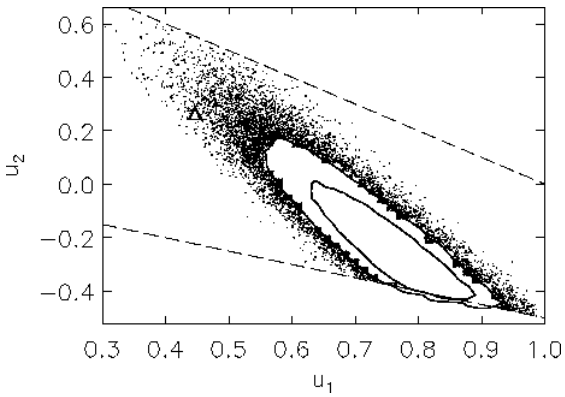

FIG. 8.— Joint posterior probability for the stellar limb darkening coefficients, u_1 and u_2. The solid contours are isoprobability contours containing 68% and 90% of the MCMC samples. The remaining 10% of the samples lying outside the region of highest probability are also shown (*points*). The region of highest probability differs from the theoretically calculated limb darkening coefficients (*triangle*). The prior limits for the limb darkening coefficients are indicated with *dashed lines*.

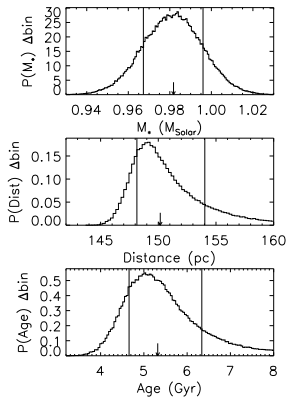

FIG. 9.— The marginalized posterior probability for the XO-2 that rely on the SME isochrone analysis. The SME isochrone analysis translates the posterior distribution for $R_\star$ into the posterior distribution for Distance and Age.

not materially affect the parameter estimates. We summarize the properties of XO-2b in Table 7.

The uncertainties given in Table 7 for XO-2b and Table 2 for XO-2 represent the precision of our experiment. These uncertainties represent the expected scatter of values obtained if the experiment was repeated with similar quality data and identical procedures. Other systematic sources of error affect the accuracy of our measurement that are most likely comparable or larger than our precision. The sources of systematic error only enter into our prior for $M_\star$. Our adopted uncertainty in $M_\star$ ∼2% follows from the uncertainty in T_{eff} and metallicity in the SME isochrone analysis (see § 3.1) aided by the very weak dependence of $M_\star$ on the unknown distance to XO-2. Hillenbrand & White (2004) show the Y^2 isochrones employed in this study successfully predict stellar masses to within 1%-3% for main sequence stars $M_\star > 0.6$ $M_\odot$ with independent dynamical mass estimates. For the derived T_{eff} and [Fe/H] for XO-2, the isochrones from Girardi et al. (2002) at maximum differ by 3% in $M_\star$ from the Y^2 isochrone prediction. Cody & Sasselov (2002) find 7% systematic error in $M_\star$ for HD 209458 due to uncertainty in Helium abundance and the treatment of convection. In light of these potential sources of systematic uncertainty, we increased the standard deviation of the Gaussian prior on $M_\star$ to $\sigma = 0.07$ $M_\odot$. This larger uncertainty on $M_\star$ resulted in more symmetric and slightly broader posterior distributions for $R_\star$ ($\sigma \pm 0.03$ $R_\odot$), R_p ($\sigma \pm 0.03$ R_J), and age ($\sigma \pm 1.4$ Gyr). The surface gravity of the planet, g_p, is independent of $M_\star$ (Southworth et al. 2007). From the measured radial velocity semi-amplitude and light curve parameters, g_p =14.8±1.6 m s^{-2} for XO-2b, where the uncertainty in g_p is dominated by the uncertainty in the radial velocity semi-amplitude. Other parameters weakly dependent on $M_\star$ and available from the light curve observations directly are $a/R_\star = 8.2\pm^{0.1}_{0.2}$ and $a/R_p = 79.0\pm^{0.9}_{2.5}$.

3.3. *Radial Velocity Measurements*

We measured the mass of XO-2b using the radial velocity technique described below and by McCullough et al. (2006). The 2-dimensional spectra obtained with the HET were extracted to 1-dimensional spectra and associated approximate wavelength solutions derived from ThAr spectra obtained during twilight (§ 2.3). To account for optical distortions, the wavelength solution fits the centroids of thousands of ThAr lines to a function of the X and Y coordinates of the CCD that includes terms linear in X and in Y plus the following cross terms: XY, XXY, XYY, XXYY, XXXY, and XYYY. Using a downhill simplex χ^2 minimization algorithm, "Amoeba," we adjusted the parameters of a synthetic spectrum to fit, in separate ∼15 Å sections, the stellar spectrum observed through an iodine absorption cell. The requirement of strong iodine lines limits radial velocity estimates to the wavelength range $5210 < \lambda < 5700$ Å. The synthetic spectrum consists of a high-resolution spectrum of the Sun, the Earth's atmosphere[13] (Wallace et al. 1998), and a high-resolution spectrum of an iodine gas cell (Cochran 2000) convolved with a Voigt profile to approximate the line-spread-function of the instrument. In addition to the convolution, we used a few additional free parameters to model specific physical or instrumental characteristics: the radial velocity of the star, a shift of the iodine spectrum attributable to instrumental errors in the approximate wavelength solution specific to the particular 15 Å section, the continuum level, and an exponent that adjusts the optical depths of the solar absorption lines in order to better approximate the (non-solar) stellar spectrum. The difference of the parameters representing the radial velocity of the star and that attributable to the instrument from the iodine spectrum equals the topocentric radial velocity of the star, which we transform to the barycentric frame of the solar system. We average the individual stellar radial velocity estimates from each of the 15 Å sections to determine the stellar radial velocity measurement at each epoch and its associated 1-σ uncertainty (see Table 3).

Figure 10 shows the resulting radial velocity curve phased with the XO-2b ephemeris determined from the transits and assuming zero eccentricity. The typical uncertainty for each measurement, $\sigma_{RV} = 20$ m s^{-1}. The radial velocity semi-amplitude, K=85±8 m s^{-1}. This amplitude results in M_p =0.57±0.06 M_J for XO-2b, assuming $M_\star$=0.98 $M_\odot$ for XO-2 and a circular orbit for XO-2b. The six radial velocities measured for XO-2S

[13] Within the wavelength range of interest, telluric absorption lines are negligible but are included anyway.

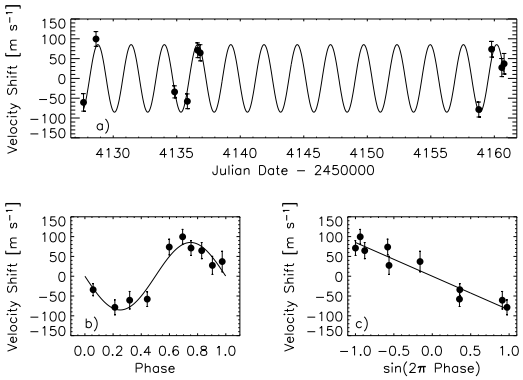

FIG. 10.— a) The radial velocity of XO-2 oscillates sinusoidally with a semi-amplitude K = 85±8 m s^{-1}, implying XO-2b's mass is 0.57±0.06 M_J. b) The period and phase of the radial velocities were fixed at values determined by the transits. The mean stellar radial velocity with respect to the solar system's barycenter has been subtracted. In order to determine K, we used the HET spectra calibrated with an iodine absorption cell (filled circles). c) In this representation of the data, a circular orbit yields a straight line of slope −K.

(Table 3) are consistent within the observational errors with no radial velocity variation and show no significant evidence for a HJ orbiting XO-2S.

3.4. *Ephemeris and Transit Timing Variations*

The database of E.T. transit light curves for XO-2b enable us to refine the ephemeris for XO-2b and to quantify transit timing variations from this ephemeris. The transit light from the 1.8m Perkins Telescope on February 16, 2007 provides a precise measurement of the mid-transit zeropoint of XO-2b. From the best fitting transit model in a χ^2 sense during the MCMC calculation, we find the ephemeris zeropoint is 2454147.74902 with an uncertainty of 17 s.

To refine the orbital period of XO-2b, we calculate mid-transit times for the nearly complete transit events observed with the XO cameras on 2453355 and 2453376 HJD and the E.T. transit events shown in Figure 3 with nearly complete ingress and egress coverage. We compare the transit data with a limb-darkened transit model. The only free parameter of the transit model is the mid-transit time. The other parameters of the transit model are fixed at the best fitting transit model in a χ^2 sense during the MCMC calculation, and the model employs theoretically calculated limb darkening coefficients obtained from Claret (2000) in the appropriate passband of the observations. The transit model has a flux decrement of $\rho^2/2$ when applied to the XO survey data to account for the transit depth dilution caused by the flux of XO-2S in the photometric aperture.

Table 6 provides the resulting mid-transit times. The three independent mid-transit estimates on 2454168 HJD enables estimating the typical uncertainty (1-σ=3 min) in the transit timing. To refine the orbital period we minimize the χ^2 difference between the transit timing observations and ephemeris model. We keep the ephemeris zeropoint fixed at the value derived from the 1.8m Perkins Telescope light curve. The best-fit period, 2.615857±0.000005 day, results in a χ^2_{min} = 10.1 for ν=11 degrees of freedom. This suggests there are no significant timing variations. For the minimization we assumed a uniform error, σ=3 min, on the transit timings. The ephemeris for XO-2b accumulates a 5 min uncertainty by 2010.

4. DISCUSSION

The transit candidate of Mandushev et al. (2005) illustrates the non-negligible potential for triple stars to have transit light curves and radial velocity variations consistent with a planet. However, in the case of XO-2b, our attempts to explain the light curve and spectroscopy with a physical stellar triple fail. We employ the Y^2 isochrone appropriate for the the physical properties of XO-2 supplemented with the low-mass stellar isochrone between 0.072< $M_\star$ <0.5 $M_\odot$ from Chabrier et al. (2000), stellar limb darkening coefficients from Claret (2000), and the light curve synthesis routine of Wilson (1993) to model a stellar triple system. The constraints on the transit duration and transit depth from the light curve require $M_\star > 0.95$ $M_\odot$ for the primary in a stellar binary blended with the light of XO-2. The required stellar binary has >75% the flux of XO-2 and has a radial velocity semi-amplitude, $K > 16$ km s^{-1}. Such a binary would be readily apparent in the spectrum of XO-2 given the narrow spectral features for XO-2, $v \sin i < 2.3$ km s^{-1}. We cannot completely rule out the possibility of a line-of-sight faint background binary blended with the light of XO-2 as an explanation for the observations. However, the sinusoidal shape of the radial velocity variations necessitate the line-of-sight binary to have a systemic velocity similar to XO-2 otherwise the radial velocity curve develops asymmetries that are not observed (Torres et al. 2005). Given the large proper motion of XO-2, ground-based adaptive optics or space-based observations have the potential to definitively rule out a background line-of-sight binary.

In addition to XO-2, only HAT-P-1, HD 20782, HD 80606, HD 99492 (GJ 429B), HD 178911B, and HD 186427 (16 Cyg B) have ΔV <2.0 mag difference between the stellar binary components (Desidera & Barbieri 2007, supplemented by data from the SIMBAD database) and can be considered nearly-equal-mass stellar binaries hosting a known extrasolar planet. In 5 out of the 7 binary systems, the planet orbits the lower mass star of the binary. In the remaining 2 systems, HD 20782 and HD 80606, the planet orbits the more massive star, but the orbits for these planets have the highest eccentricities amongst all known planets, e=0.93 and e=0.92, respectively (Butler et al. 2006). Equivalently, if we restrict the sample of extrasolar planets in nearly-equal-mass stellar binaries to modest eccentricity (e<0.8), in 5 of the 5 known systems, the planet orbits the lower mass star. We offer several speculative possibilities to explain the current pattern of planets in nearly-equal-mass stellar binaries: 1) The pattern arises due to small sample statistics, 2) Planets form more readily around the lower mass component of a nearly-equal-mass stellar binary, 3) Planets form equally likely around the components of a nearly-equal-mass stellar binary, but planets orbiting the primary component have lower detectability due to lower planet mass or higher orbital eccentricity (Cumming 2004).

The XO-2 stellar binary has a higher space velocity with respect to the Local Standard of Rest (LSR), $v = \sqrt{U^2 + V^2 + W^2} \sim 100$ kms^{-1}, than most of the other known extrasolar planets (Santos et al.

2003; Ecuvillon et al. 2007). According to the purely kinematic classification of Bensby et al. (2003) and Bensby et al. (2006), XO-2 has ∼7 times higher probability of belonging to the Thick Disk than the Thin Disk. From a chemical abundance perspective, a metallicity of [Fe/H]< -0.3 is typically the upper limit for Thick Disk metallicities (Mishenina et al. 2004; Reddy et al. 2006). However, Bensby et al. (2006) has recently claimed kinematically selected Thick Disk stars with [Fe/H]$\sim$ 0.0 have a chemical abundance pattern distinguishable from Thin Disk stars at the same metallicity. The sample of stars with kinematics suggestive of the Thick Disk but Thin Disk metallicities, like XO-2, is still too small to determine their relationship to the traditional Thin/Thick Disk populations. However, Mishenina et al. (2004) distinguishes between objects with Thick Disk kinematics and Thin Disk metallicity by determining the maximum height above the Galactic disk their orbit attains, Z_{max}. Both the estimate of Bensby et al. (2005) for Z_{max} and integrating the orbit of XO-2 using the axi-symmetric, static Galaxy potential model of Allen & Santillan (1991) yield $Z_{max} \sim 100$ pc for the orbit of XO-2. Given the much larger scale height for the Thick Disk, $\sigma_{TD} \sim 1000$ kpc, under the classification of Mishenina et al. (2004), XO-2 belongs to the Thin Disk, since its orbit is well confined to the Galactic plane. The high space velocity of XO-2 results from high eccentricity rather than excursions from Galactic plane. Using the simple model from Allen & Santillan (1991), the orbit of XO-2 has a pericenter within ∼4 kpc of the Galactic center and apocenter ∼9 kpc (e∼0.4).

Currently, XO-2 lags the LSR by $V = -78$ kms^{-1} and is moving away from the Galactic center at $U = -71$ kms^{-1}. This places XO-2 in phase space near the Hercules stream (Famaey et al. 2005; Ecuvillon et al. 2007) ($U = 42$, $\sigma_U = 28$, $V = -52$, $\sigma_V = 9$ kms^{-1}), but is lagging the LSR more than the typical Hercules stream member. The possibility that XO-2 belongs to a dynamical stream originating from the metal-rich inner Galaxy is an example that supports the findings of Famaey et al. (2005) and Ecuvillon et al. (2007) that compared to field stars, metal-enhanced dynamical streams should be overabundant in detectable extrasolar planets.

5. SUMMARY

The star XO-2, GSC 34130-0005, hosts an approximately Jupiter-size, 0.6 Jupiter-mass transiting extrasolar planet, XO-2b, with an orbital period ∼2.6 days. XO-2 is a V=11.2 early K dwarf with high metallicity, [Fe/H]=0.45, high proper motion, $\mu_{tot} = 157$ mas yr^{-1}, and has a common proper motion stellar companion with 31″ separation. The followup high resolution spectroscopy yields $M_\star$=0.98±0.02 M$_\odot$ for the mass of XO-2 and M_p=0.57±0.06 M$_J$ for the mass of XO-2b. The followup high precision photometry yields $R_\star$=$0.97\pm^{0.02}_{0.01}$ R$_\odot$ for the radius of XO-2 and R_p=$0.98\pm^{0.03}_{0.01}$ R$_J$ for the radius of XO-2b. Joint analysis of the light curve and spectroscopy yields an isochrone based age of XO-2 t=$5.3\pm^{1.0}_{0.7}$ Gyr, and an isochrone based distance to XO-2 d=$150\pm^{4}_{2}$ pc. The quoted values and their uncertainties are Bayesian credible intervals encompassing 68% of the marginalized posterior probability. For the Bayesian analysis we assume a Gaussian-like prior on $M_\star$, derived from the spectroscopic and isochrone analysis of XO-2 and uniform priors on $R_\star$, R_p, orbital inclination, and limb darkening coefficients. We describe an efficient Markov Chain Monte Carlo method to calculate the Bayesian posterior probability for the system parameters from a transit light curve.

XO-2b adds to the sample of Jupiter-mass planets residing in nearly-equal-mass stellar binaries. In 5 of the 7 nearly-equal-mass stellar binaries hosting a planet, the planet orbits the lower mass stellar component. In the remaining 2 stellar binaries where the planet orbits the higher mass star, the planets' orbits are highly eccentric (e>0.9). Equivalently, if we restrict the sample of extrasolar planets with modest eccentricity (e<0.8) orbits in nearly-equal-mass stellar binaries, in 5 of the 5 known systems, the planet orbits the lower mass star. We speculate on possible astrophysical reasons for this pattern beyond the simple fact that the statistics are based upon a very small sample and thus may be spurious.

With its high proper motion, XO-2 has kinematics suggestive of Thick Disk membership but a Thin Disk metallicity. In contrast to the typical Thick Disk member, the high proper motion of XO-2 results from an eccentric orbit (Galactic pericenter, $R_{per} < 4$ kpc) well confined to the Galactic disk, $Z_{max} \sim 100$ pc. XO-2 may originate in the metal-rich inner Thin Disk and was dynamically scattered into the solar neighborhood. Similar to the findings of Famaey et al. (2005) and Ecuvillon et al. (2007), the discovery of XO-2b suggests metal-enhanced dynamical streams from the inner Galaxy may be abundant in detectable extrasolar planets.

The University of Hawaii staff have made the operation on Maui possible; we thank especially Jake Kamibayashi, Bill Giebink, Les Hieda, Jeff Kuhn, Haosheng Lin, Mike Maberry, Daniel O'Gara, Joey Perreira, Kaila Rhoden, and the director of the IFA, Rolf-Peter Kudritzki. The Hobby-Eberly Telescope (HET) is a joint project of the University of Texas at Austin, the Pennsylvania State University, Stanford University, Ludwig-Maximilians-Universität München, and Georg-August-Universität Göttingen. The HET is named in honor of its principal benefactors, William P. Hobby and Robert E. Eberly. We thank the HET night-time and day-time support staff and the Resident Astronomer telescope operator; we especially thank John Caldwell, Frank Deglman, Heinz Edelmann, Stephen Odewahn, Vicki Riley, Sergey Rostopchin, Matthew Shetrone, and Chevo Terrazas.

We thank Dave Healy, Lisa Prato, and Marcos Huerta for assistance observing. We acknowledge helpful discussions with Julio Chaname, Ron Gilliland, and Zheng Zheng. We thank the referee for the insightful suggestions and significant improvements to the manuscript.

This research has made use of the SIMBAD database, operated at CDS, Strasbourg, France; data products from the Two Micron All Sky Survey (2MASS), the Digitized Sky Survey (DSS), and The Amateur Sky Survey (TASS); source code for transit light-curves (Mandel & Agol 2002); and community access to the HET.

XO is funded primarily by NASA Origins grant NNG06GG92G and the Director's Discretionary Fund of the STScI.

APPENDIX

MARKOV CHAIN MONTE CARLO DETAILS

Care must be taken to properly assign prior probabilities for a nonlinear transformation in parameters (Chu et al. 2003). In particular, a uniform prior in i is not the same as a uniform prior in τ. The transformation law of probabilities provides the necessary prior probability to maintain the uniform prior in $R_\star$, R_p, and i for our chosen set of free parameters: $R_\star$, ρ, and τ, where

$$\tau = \frac{P}{\pi}\arcsin\left(\frac{R_\star}{a}\left[\frac{(1+\rho)^2-(a/R_\star\cos i)^2}{1-\cos i^2}\right]^{1/2}\right), \tag{A1}$$

where P is the orbital period, a is the semi-major axis, and we have assumed zero eccentricity (Seager & Mallén-Ornelas 2003).

The general transformation law with multiple dimensions states

$$p(y_1, y_2, ...)dy_1dy_2... = p(x_1, x_2, ...)\left\|\frac{\partial(x_1, x_2, ...)}{\partial(y_1, y_2, ...)}\right\| dy_1dy_2..., \tag{A2}$$

where the original joint probability distribution, $p(x_1, x_2, ...)dx_1dx_2...$, is transformed into another probability distribution in terms of the new set of variables $(y_1, y_2, ...)$ by multiplication with the absolute value of the Jacobian determinant, $\|\partial()/\partial()\|$. The new y variables must have the same number and be expressible in terms of the old x variables (Press et al. 1992). Writing the old variables in terms of the new variables, $R_\star = R'_\star$, $R_p = \rho R'_\star$, and

$$i = \arccos\sqrt{\frac{(R'_\star/a)^2(1+\rho)^2-\sin\phi^2}{(1-\sin\phi^2)}}, \tag{A3}$$

where $\phi = \tau\pi/P$, the Jacobian matrix is written

$$\|\partial()/\partial()\| = \left\|\begin{matrix} \frac{\partial R_\star}{\partial R'_\star}=1 & \frac{\partial R_\star}{\partial \rho}=0 & \frac{\partial R_\star}{\partial \tau}=0 \\ \frac{\partial R_p}{\partial R'_\star} & \frac{\partial R_p}{\partial \rho} & \frac{\partial R_p}{\partial \tau}=0 \\ \frac{\partial i}{\partial R'_\star} & \frac{\partial i}{\partial \rho} & \frac{\partial i}{\partial \tau} \end{matrix}\right\|, \tag{A4}$$

where we have indicated the trivial elements with value one or zero. Overall, the Jacobian simplifies to

$$|(\partial R_p/\partial\rho)(\partial i/\partial\tau)| = \frac{\pi}{P}R'_\star\sin\phi\sqrt{\frac{((R'_\star/a)^2(1+\rho)^2-1)}{(\sin\phi^2-(R'_\star/a)^2(1+\rho)^2)}}. \tag{A5}$$

With our choice of parameters, the proper prior to maintain uniform priors in $R_\star$, R_p, and i is the above Jacobian multiplied by the original joint probability distribution for uniform priors, which is a constant. The prior probability goes to zero for $0 < \tau < \tau_{max}$, where $\tau_{max} = P/\pi\arcsin(R_\star/a)(1+\rho)$.

A trial chain is necessary to define the covariance matrix for the final eigenbasis set of parameters. $M_\star$, $R_\star$, ρ, τ, u_1, and u_2 enter into the covariance matrix. We find t_o shows no significant correlation with respect to the other parameters. To determine the necessary linear transformation, we determine the eigenvectors of the covariance matrix built from a trial chain (Tegmark et al. 2004). This is equivalent to a Principal Component Analysis. The bottom panels in Figure 6 show trial samples in terms of the eigenvectors of the covariance matrix. The eigenvector along the largest variance, e_1, is predominately along $R_\star$, and e_2 and e_3 are a mixture of ρ and τ.

The autocorrelation length of samples in the MCMC sequence is one method to quantify the efficiency of the calculation. With the original set of parameters ($R_\star$, R_p, and i), the correlation length (when the autocorrelation drops by half) in the $R_\star$ parameter varied, $500 < N_{cor} < 1500$ steps. Using our new set of parameters ($R_\star$, ρ, and τ), $40 < N_{cor} < 60$ steps. Finally, with the eigenbasis parameters, $4 < N_{cor} < 5$ steps, where the correlation is measured in the physical variable $R_\star$.

REFERENCES

Allen, C., & Santillan, A. 1991, Revista Mexicana de Astronomia y Astrofisica, 22, 255

Bakos, G. Á., et al. 2007, ApJ, 656, 552

Bensby, T., Feltzing, S., & Lundström, I. 2003, A&A, 410, 527

Bensby, T., Feltzing, S., Lundström, I., & Ilyin, I. 2005, A&A, 433, 185

Bensby, T., Zenn, A. R., Oey, M. S., & Feltzing, S. 2006, in ASP Conf. Ser., From stars to galaxies: Building the pieces to build up the Universe, ed. A. Vallenari, R. Tantali, L. Portinari, A. Moretti (San Francisco:ASP), in press (astro-ph/0612459)

Benz, W., Alibert, Y., Mordasini, C., & Naef, D. 2006, IAU Colloq. 200: Direct Imaging of Exoplanets: Science & Techniques, 1

Bessell, M. S. 2000, PASP, 112, 961

Bodenheimer, P., Laughlin, G., & Lin, D. N. C. 2003, ApJ, 592, 555

Burrows, A., Hubeny, I., Budaj, J., & Hubbard, W. B. 2006, preprint (astro-ph/0612703)

Burke, C. J., Gaudi, B. S., DePoy, D. L., & Pogge, R. W. 2006, AJ, 132, 210

Butler, R. P., et al. 2006, ApJ, 646, 505

Cameron, A. C., et al. 2007, MNRAS, 375, 951

Chabrier, G., Baraffe, I., Allard, F., & Hauschildt, P. 2000, ApJ, 542, 464

Charbonneau, D., Brown, T. M., Latham, D. W., & Mayor, M. 2000, ApJ, 529, L45

Charbonneau, D., Brown, T. M., Noyes, R. W., & Gilliland, R. L. 2002, ApJ, 568, 377
Charbonneau, D., et al. 2005, ApJ, 626, 523
Charbonneau, D., Brown, T. M., Burrows, A., & Laughlin, G. 2007, Protostars and Planets V, 701
Charbonneau, D., Winn, J. N., Everett, M. E., Latham, D. W., Holman, M. J., Esquerdo, G. A., & O'Donovan, F. T. 2007, ApJ, 658, 1322
Chu, M., Kaplinghat, M., & Knox, L. 2003, ApJ, 596, 725
Claret, A. 2000, A&A, 363, 1081
Cochran, W. 2000, FTS Spectrum of I2 Cell HRS3 At 69.9 C., ftp://nsokp.nso.edu/FTS_cdrom/FTS50/001023R0.004
Cody, A. M., & Sasselov, D. D. 2002, ApJ, 569, 451
Cumming, A., Marcy, G. W., & Butler, R. P. 1999, ApJ, 526, 890
Cumming, A. 2004, MNRAS, 354, 1165
Deming, D., Seager, S., Richardson, L. J., & Harrington, J. 2005, Nature, 434, 740
Desidera, S., & Barbieri, M. 2007, A&A, 462, 345
Dravins, D., Lindegren, L., Mezey, E., & Young, A. T. 1997, PASP, 109, 173
Ecuvillon, A., Israelian, G., Pont, F., Santos, N. C., & Mayor, M. 2007, A&A, 461, 171
Famaey, B., Jorissen, A., Luri, X., Mayor, M., Udry, S., Dejonghe, H., & Turon, C. 2005, ESA SP-576: The Three-Dimensional Universe with Gaia, 129
Fischer, D. A., & Valenti, J. 2005, ApJ, 622, 1102
Ford, E. B. 2005, AJ, 129, 1706
Fortney, J. J., Saumon, D., Marley, M. S., Lodders, K., & Freedman, R. S. 2006, ApJ, 642, 495
Gaudi, B. S. 2000, ApJ, 539, L59
Gelman, A., & Rubin, D. B. 1992, Stat. Sci., 7, 457
Girardi, L., Bertelli, G., Bressan, A., Chiosi, C., Groenewegen, M. A. T., Marigo, P., Salasnich, B., & Weiss, A. 2002, A&A, 391, 195
Gonzalez, G. 2006, PASP, 118, 1494
Gregory, P. C. 2005, ApJ, 631, 1198
Grillmair, C. J., Charbonneau, D., Burrows, A., Armus, L., Stauffer, J., Meadows, V., Van Cleve, J., & Levine, D. 2007, ApJ, 658, L115
Guillot, T., & Showman, A. P. 2002, A&A, 385, 156
Guillot, T., Santos, N. C., Pont, F., Iro, N., Melo, C., & Ribas, I. 2006, A&A, 453, L21
Harrington, J., Hansen, B. M., Luszcz, S. H., Seager, S., Deming, D., Menou, K., Cho, J. Y.-K., & Richardson, L. J. 2006, Science, 314, 623
Henry, G. W., Marcy, G. W., Butler, R. P., & Vogt, S. S. 2000, ApJ, 529, L41
Hillenbrand, L. A., & White, R. J. 2004, ApJ, 604, 741
Hinkle, K. H., Joyce, R. R., Sharp, N., & Valenti, J. A. 2000, Proc. SPIE, 4008, 720
Høg, E., et al. 2000, A&A, 355, L27
Holman, M. J., & Wiegert, P. A. 1999, AJ, 117, 621
Holman, M. J., et al. 2006, ApJ, 652, 1715
Ida, S., & Lin, D. N. C. 2004, ApJ, 616, 567
Kosowsky, A., Milosavljevic, M., & Jimenez, R. 2002, Phys. Rev. D, 66, 063007
Kovács, G., Zucker, S., & Mazeh, T. 2002, A&A, 391, 369
Kurucz, R. L. 1992, IAU Symp. 149, The Stellar Populations of Galaxies, ed. B. Barbuy & A. Renzini (Dordrecht: Reidel), 225
Kurucz, R. L. 1993, SYNTHE Spectrum Synthesis Programs and Line Data (Kurucz CD-ROM No. 18) (Cambridge: SAO)
Janes, K. A., Clemens, D. P., Hayes-Gehrke, M. N., Eastman, J. D., Sarcia, D. S., & Bosh, A. S. 2004, Bulletin of the American Astronomical Society, 36, 672
Landolt, A. U. 1992, AJ, 104, 340
Lépine, S., & Shara, M. M. 2005, AJ, 129, 1483
Lewis, A., & Bridle, S. 2002, Phys. Rev. D, 66, 103511
Malmberg, D., Davies, M. B., & Chambers, J. E. 2007, MNRAS, L18
Mamajek, E. E., Meyer, M. R., & Liebert, J. 2002, AJ, 124, 1670
Mandel, K., & Agol, E. 2002, ApJ, 580, L171
Mandushev, G., et al. 2005, ApJ, 621, 1061
J., Seager, S., & Barman, T. 2007, Protostars and Planets V, 733
Marzari, F., & Barbieri, M. 2007, A&A, in press (astro-ph/0702342)
McCullough, P. R., Stys, J. E., Valenti, J. A., Fleming, S. W., Janes, K. A., & Heasley, J. N. 2005, PASP, 117, 783
McCullough, P. R., et al. 2006, ApJ, 648, 1228
McCullough, P. R., & Burke, C. J. 2007, ASP Conf. Ser., Transiting Extrasolar Planets Workshop, ed. C. Afonso, D. Weldrake, & T. Henning (San Francisco:ASP), in press (astro-ph/0703331)
Mihalas, D., & Binney, J. 1981, Galactic Astronomy: Structure and Kinematics (2nd ed., San Francisco: W. H. Freeman and Co.)
Mishenina, T. V., Soubiran, C., Kovtyukh, V. V., & Korotin, S. A. 2004, A&A, 418, 551
Muller, D. E. 1956, Mathematical Tables and Other Aids to Computations, 10, 208
Neal, R. M. 2003, Annals of Statistics, 31, 705
Nordström, B., et al. 2004, A&A, 418, 989
Piskunov, N. E., Kupka, F., Ryabchikova, T. A., Weiss, W. W., & Jeffery, C. S. 1995, A&AS, 112, 525
Press, W. H., Teukolsky, S. A., Vetterling, W. T., & Flannery, B. P. 1992, Cambridge: University Press, —c1992, 2nd ed.
Raghavan, D., Henry, T. J., Mason, B. D., Subasavage, J. P., Jao, W.-C., Beaulieu, T. D., & Hambly, N. C. 2006, ApJ, 646, 523
Reddy, B. E., Lambert, D. L., & Allende Prieto, C. 2006, MNRAS, 367, 1329
Santos, N. C., Israelian, G., Mayor, M., Rebolo, R., & Udry, S. 2003, A&A, 398, 363
Sato, B., et al. 2005, ApJ, 633, 465
Schuler, S. C., Hatzes, A. P., King, J. R., Kürster, M., & The, L.-S. 2006, AJ, 131, 1057
Seager, S., & Mallén-Ornelas, G. 2003, ApJ, 585, 1038
Skrutskie, M. F., et al. 2006, AJ, 131, 1163
Southworth, J., Wheatley, P. J., & Sams, G. 2007, MNRAS, 379, L11
Tamuz, O., Mazeh, T., & Zucker, S. 2005, MNRAS, 356, 1466
Tegmark, M., et al. 2004, Phys. Rev. D, 69, 103501
Torres, G., Konacki, M., Sasselov, D. D., & Jha, S. 2005, ApJ, 619, 558
Tull, R. G., MacQueen, P. J., Sneden, C., & Lambert, D. L. 1995, PASP, 107, 251
Tull, R. G. 1998, Proc. SPIE, 3355, 387
Valenti, J. A., & Fischer, D. A. 2005, ApJS, 159, 141
Valenti, J. A., & Piskunov, N. 1996, A&AS, 118, 595
Wallace, L., Hinkle, K., & Livingston, W. 1998, An atlas of the spectrum of the solar photosphere from 13,500 to 28,000 cm-1 (3570 to 7405 A), (Tucson, AZ: NOAO)
Wilson, R. E. 1993, New Frontiers in Binary Star Research, 38, 91
Winn, J. N., & Holman, M. J. 2005, ApJ, 628, L159
Yi, S., Demarque, P., Kim, Y.-C., Lee, Y.-W., Ree, C. H., Lejeune, T., & Barnes, S. 2001, ApJS, 136, 417

TABLE 1
XO Survey & E.T. Light Curve Data[a]

Heliocentric Julian Date	Light Curve [mag]	Uncertainty (1-σ) [mag]	Filter	N[b]	Observatory
2452961.14380	-0.0027	0.0039	W	1	XO
2452961.14404	-0.0002	0.0037	W	1	XO
2452964.11621	-0.0057	0.0034	W	1	XO
2452964.11646	-0.0018	0.0033	W	1	XO
2452964.12329	0.0034	0.0034	W	1	XO

[a] The complete version of this table is in the electronic edition of the Journal. The printed edition contains only a sample.
[b] Average of N measurements

TABLE 2
Stellar Properties

Parameter	XO-2N	XO-2S	Reference
GSC ID	03413-00005	03413-00210	a
RA (J2000.0)	$7^h48^m06^s.47$	$7^h48^m07^s.48$	a,b
Dec (J2000.0)	$+50°13'33''.0$	$+50°13'03''.3$	a,b
Galactic Latitude b [deg]	29.33	...	a
" Longitude l [deg]	168.29	...	a
V	11.18±0.03	11.12±0.03	c
(B-V)	0.82±0.05	0.79±0.05	c
(V-R_c)	0.49±0.05	0.46±0.05	c
(V-I_c)	0.86±0.05	0.82±0.05	c
V_T	11.24	11.20	b,d
$(B-V)_T$	0.70	0.86	b,d
J	9.74±0.02	9.74±0.02	e
(J-H)	0.40±0.03	0.37±0.03	e
(H-K)	0.03±0.03	0.10±0.03	e
Spectral Type	K0V	K0V	c
Distance [pc]	$150\pm^{4}_{2}$	...	c
μ_α [mas yr^{-1}]	-34.7±2.6	-33.1±2.9	b
μ_δ [mas yr^{-1}]	-153.6±2.4	-154.1±2.7	b
Total μ[mas yr^{-1}]	157	158	f
Radial Velocity (Bary) [km s^{-1}]	47.4±0.5	...	c
U Space Velocity [km s^{-1}]	-72.0	...	b,c,g,h
V "	-78.0	...	b,c,g
W "	-4.6	...	b,c,g
Stellar Mass [$M_\odot$]	0.98±0.02	...	c
Stellar Radius [$R_\odot$]	$0.97\pm^{0.02}_{0.01}$	...	c

References:
a) SIMBAD
b) Tycho-2 (Høg et al. 2000)
c) this work
d) Tycho-2 photometry on the Johnson system (Bessell 2000; Mamajek et al. 2002)
e) 2MASS (Skrutskie et al. 2006)
f) LSPM (Lépine & Shara 2005)
g) Space Velocity w.r.t. LSR after correction for Solar peculiar motion (Mihalas & Binney 1981).
h) Negative U is away from the Galactic Center

TABLE 3
Radial Velocity Shifts

Object	Julian Date -245000	Radial Velocity Shift [m s^{-1}]	Uncertainty (1-σ) [m s^{-1}]
XO-2N			
	4127.6626	-60.6	22
	4128.6459	99.5	18
	4134.8318	-34.0	15
	4135.8366	-57.8	19
	4136.6494	71.0	19
	4136.8477	64.6	20
	4158.7782	-78.5	19
	4159.7882	73.6	20
	4160.5891	27.3	23
	4160.7715	37.0	26
XO-2S			
	4133.6383	-21.6	18
	4134.6257	-1.5	15
	4135.8481	-32.4	20
	4136.8599	-7.6	17
	4158.7932	30.6	17
	4168.7572	16.7	17

TABLE 4
Results of the SME Analysis

Parameter	XO-2N	XO-2S	Uncertainty (1-σ)	Uncertainty (99.7%)
T_{eff} [K]	5340	5500	32	233
log$g$ [cm s^{-2}]	4.48	4.62	0.05	0.36
v sin i [km s^{-1}]	1.4	1.2	0.3	2.1
[M/H]	0.44	0.45	0.02	0.20
[Na/H]	0.49	0.63	0.02	0.18
[Si/H]	0.39	0.47	0.02	0.12
[Ti/H]	0.36	0.42	0.04	0.26
[Fe/H]	0.45	0.47	0.02	0.22
[Ni/H]	0.50	0.52	0.02	0.16
[Si/Fe]	-0.06	0.00	0.03	0.25

TABLE 5
Spectroscopically Derived Stellar parameters

Parameter	@ 140 pc	@ 150 pc	@ 170 pc
	0.98	0.97	0.96
Mass [M$_\odot$]	0.99	0.98	0.98
	1.00	1.00	0.99
	0.90	0.95	1.07
Radius [R$_\odot$]	0.91	0.97	1.10
	0.93	0.98	1.12
	4.49	4.42	4.32
Log(g) [cm s^{-2}]	4.51	4.45	4.34
	4.53	4.48	4.37
	0.77	3.55	8.35
Age [Gyr]	2.04	5.27	9.49
	3.68	6.92	10.62

For each parameter, the middle row is the maximum likelihood value, and the values in the rows above and below span the 68% likelihood of the probability distributions (cf. Figure 5). The three columns correspond to three assumed distances for XO-2.

TABLE 6
Mid-Transit Times

Heliocentric Julian Date[a] -2450000	Observatory ID[b]
3355.14209	XO
3376.07349	XO
4126.82324	MF
4126.82324	BG
4134.66992	MF
4142.51660	EM
4147.75049	BG
4160.82812	BG
4168.67578	BG
4168.68066	CF
4168.67871	MF

[a] Based upon independent observations on 2454168 HJD, uncertainty in mid-transit time, σ=3 min.
[b] Observatory ID is author initials, except XO is XO survey data.

TABLE 7
The Planet XO-2b

Parameter	Value
P	2.615857±0.000005 d
t_c	2454147.74902±0.0002 (HJD)
K	85±8 m s^{-1}
a	0.0369±0.0002 A.U.
i	88.9±0.7 deg
M_p	0.57±0.06 M_J
R_p	$0.98\pm^{0.03}_{0.01}$ R_J
g_p	14.8±1.6m s^{-2}